JACS
JOURNAL OF THE AMERICAN CHEMICAL SOCIETY
pubs.acs.org/JACS
Article

Ultrasmall Magneto-chiral Cobalt Hydroxide Nanoparticles Enable Dynamic Detection of Reactive Oxygen Species *in Vivo*

Chen Li,[#] Si Li,[#] Jing Zhao,[#] Maozhong Sun, Weiwei Wang, Meiru Lu, Aihua Qu, Changlong Hao, Chen Chen, Chuanlai Xu,* Hua Kuang, and Liguang Xu*

Cite This: *J. Am. Chem. Soc.* 2022, 144, 1580–1588
Read Online

ABSTRACT: Biological application of chiral nanoparticles (NPs) has aroused enormous levels of attention over recent years. Here, we synthesized magneto-chiral cobalt hydroxide ($Co(OH)_2$) NPs that exhibited strong chiroptical and unique magnetic properties and applied these NPs to detect and monitor reactive oxygen species (ROS) in living cells and *in vivo*. Circular dichroism (CD) and magnetic resonance imaging (MRI) signals of the magneto-chiral $Co(OH)_2$ NPs exhibited a wide intracellular ROS detection range from 0.673 to 612.971 pmol/10^6 cells with corresponding limits of detection (LOD) at 0.087 and 0.179 pmol/10^6 cells, far below that of currently available probes; the LOD for D-aspartic acid coated $Co(OH)_2$ NPs (D-$Co(OH)_2$ NPs) was 5.7 times lower than that for L-aspartic acid coated $Co(OH)_2$ NPs (L-$Co(OH)_2$ NPs) based on the CD signals. In addition, D-$Co(OH)_2$ NPs also exhibited dynamic ROS monitoring ability. The high levels of selectivity and sensitivity to ROS in complex biological environments can be attributed to the Co^{2+} oxidation reaction on the surface of the NPs. Furthermore, magneto-chiral $Co(OH)_2$ NPs were able to quantify the levels of ROS in living mice by fluorescence and MRI signals. Collectively, these results reveal that magneto-chiral $Co(OH)_2$ NPs exhibit a remarkable ability to quantify ROS levels in living organisms, and could therefore provide new tools for exploring chiral nanomaterials as a potential biosensor to investigate biological events.

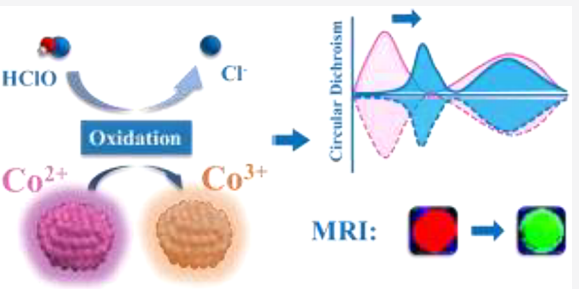

INTRODUCTION

As important signaling molecules, reactive oxygen species (ROS) are usually produced in various metabolic processes and play a vital role in regulating a diverse array of physiological functions. ROS can exist in many different forms, including hypochlorite acid (HClO), superoxide (O_2^-), hydroxyl radicals (·OH), hydrogen peroxide (H_2O_2), and singlet oxygen.[1] Yet, the potentially serious cell damage that can be caused by strong oxidation to proteins, lipids, and nucleic acids have made ROS a double-edged sword for living organisms. Overaccumulation of ROS can trigger oxidative stress and is correlated with many different pathological conditions, including cancer, neurological disorders, and cardiovascular disease.[2] Thus, to elucidate the biological roles of ROS, quantify their real-time levels, and investigate their molecular mechanisms, it is vital that we develop effective probes to monitor ROS; such probes could provide us with new research tools and clinical diagnostics.[3−10] The development of fluorescence-based probes for profiling ROS represents a significant challenge in chemical biology, and the application of organic fluorescent probes is generally acknowledged as a common strategy for ROS detection. However, these probes are vulnerable to photobleaching, spontaneous autoxidation, and biotoxicity, thus significantly reducing their potential application.[11−15] Consequently, there is a real need to develop new probes with improved performance for the detection of ROS although this remains a significant challenge in the field of chemistry.[16−21]

Chiroptical activity, as a nascent optical property of nanomaterials, has drawn significant levels of attention over the past few years[22−29] and can produce a susceptible signal response to external changes.[30−33] As such, chiroptical activity has been promoted widely for chiral analysis and detection, along with enantioselective separation.[34−40] However, the responsiveness of monodisperse chiral inorganic nanomaterials to biological signaling molecules, such as ROS, and their direct application as biosensors for real-time monitoring, has yet to be elucidated.

Herein, we report for the first time that chiral $Co(OH)_2$ NPs fabricated under gentle conditions exhibit superior CD and MRI dual signals that are selectively and sensitively responsive to ROS. Furthermore, D-$Co(OH)_2$ NPs exhibited higher performance with regards to the detection of cellular ROS

Received: September 20, 2021
Published: January 21, 2022

https://doi.org/10.1021/jacs.1c09986
J. Am. Chem. Soc. 2022, 144, 1580−1588

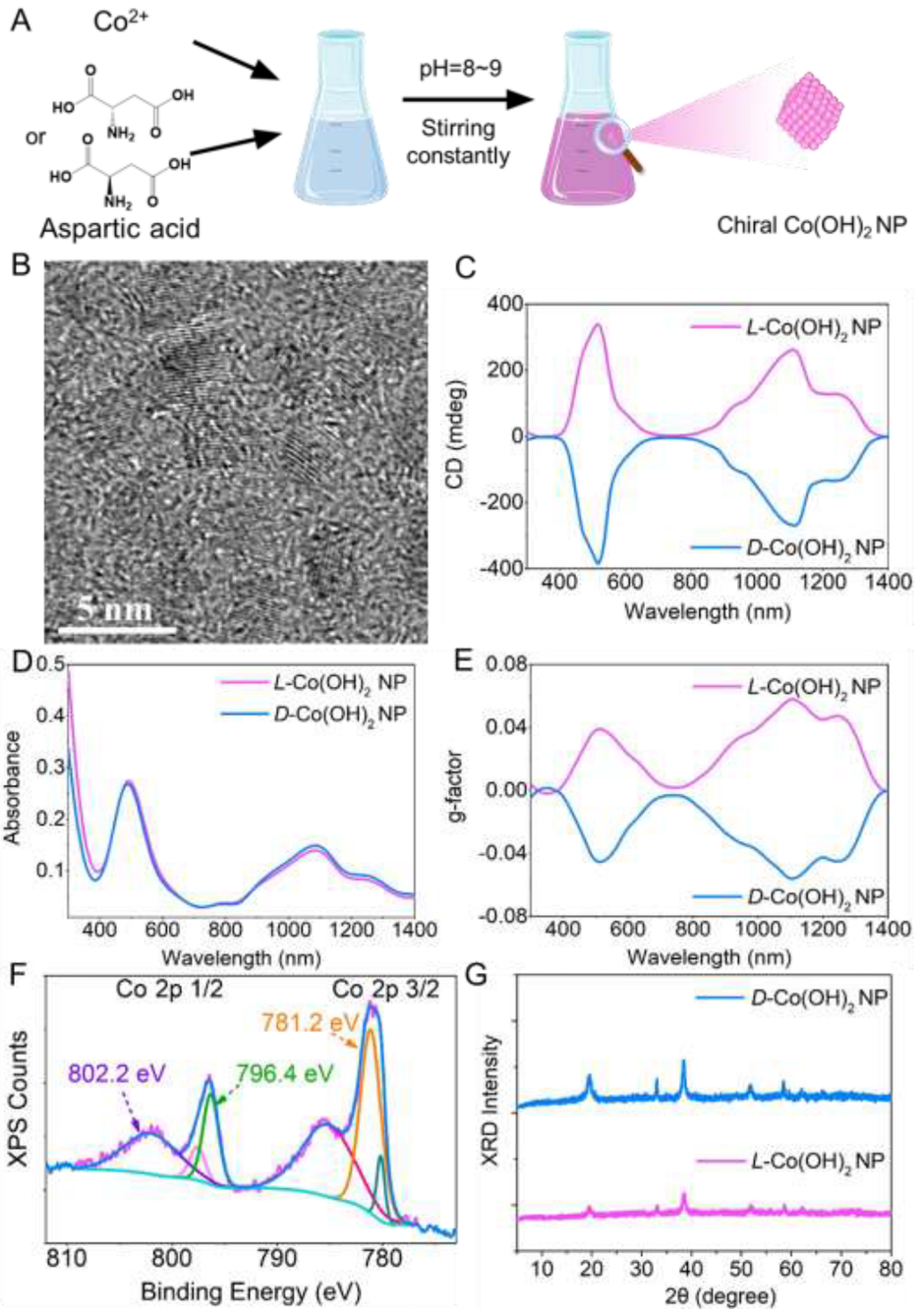

Figure 1. (A) Scheme illustration of chiral $Co(OH)_2$ NP for synthesis, termed as L-$Co(OH)_2$ NP and D-$Co(OH)_2$ NP, respectively. (B) TEM image of D-$Co(OH)_2$ NP. (C) CD, (D) UV−vis, (E) *g*-factor spectra of chiral $Co(OH)_2$ NP, (F) XPS spectra of the cobalt element in D-$Co(OH)_2$ NP, including of three typical binding energy peaks at 781.2 eV (Co^{2+} 2p 3/2), 796.4 eV (Co^{2+} 2p 1/2) and 802.2 eV (Co^{2+} 2p 1/2). (G) XRD spectra of chiral $Co(OH)_2$ NP.

cellular detection than L-$Co(OH)_2$ NPs. Finally, we decorated chiral $Co(OH)_2$ NPs with a fluorescent molecule (Alexa Fluor 568 (AF568)) to create dual-mode nanoprobes based on fluorescence and MRI signals, to quantify ROS in tumor-bearing mice.

RESULTS AND DISCUSSION

Synthesis and Characterization of Chiral $Co(OH)_2$ NPs. We used the amino acid mediated room temperature one-step synthesis method to obtain chiral $Co(OH)_2$ NPs (Figure 1A). Briefly, L-aspartic acid (L-ASP) or D-aspartic acid (D-ASP) was applied to coordinate with $CoCl_2$ to form the Co^{2+}−ASP complex. Subsequently, the NaOH solution was added to induce the nucleation process. The color of the solution gradually changed from pink to light purple-pink, thus signaling the synthesis of chiral $Co(OH)_2$ NPs.

Transmission electron microscopy (TEM) showed that the mean diameter of the chiral $Co(OH)_2$ NPs was approximately 3 nm (Figures 1B and S1A). Dynamic light scattering (DLS) spectra showed that the hydrodynamic size of the chiral $Co(OH)_2$ NPs was approximately 4 nm (Figure S1B), which was slightly larger than the core size. Energy dispersive spectrometer mapping showed that Co, O, and N elements coexisted in the chiral $Co(OH)_2$ NPs (Figure S2). The CD

https://doi.org/10.1021/jacs.1c09986
J. Am. Chem. Soc. 2022, 144, 1580−1588

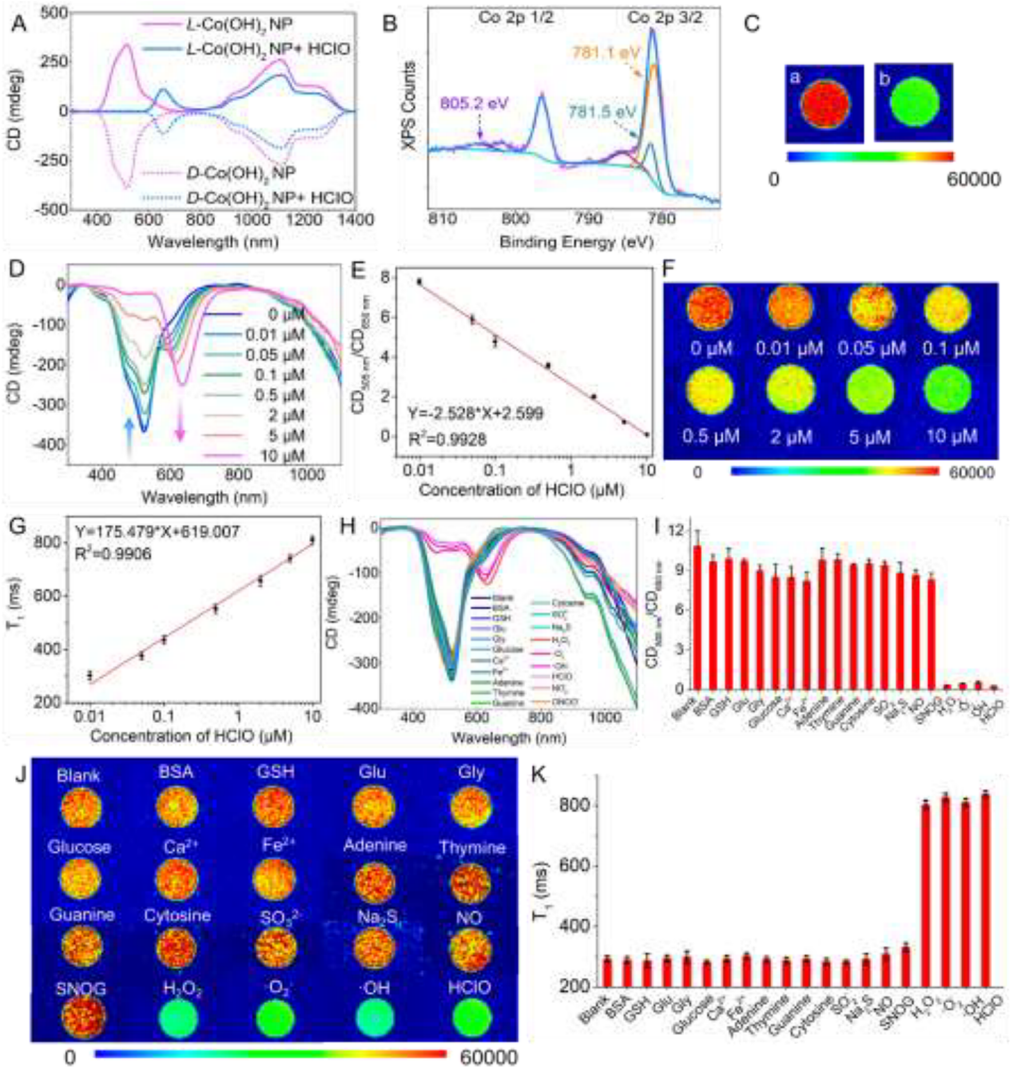

Figure 2. Responsiveness of chiral $Co(OH)_2$ NP to ROS. (A) CD spectra of chiral $Co(OH)_2$ NP before and after reacting with HClO. (B) XPS spectra of the cobalt element in D-$Co(OH)_2$ NP after reacting with HClO, including three typical binding energy peaks at 781.1 eV (Co^{3+} 2p 3/2), 781.5 eV (Co^{3+} 2p 3/2), and 805.2 eV (Co^{3+} 2p 1/2). (C) T_1-weighted MRI images of D-$Co(OH)_2$ NP (a) before and (b) after reacting with HClO. Dual-mode detection of HClO by CD and T_1-MRI signal based on the D-$Co(OH)_2$ NP *in vitro*: (D) CD spectra and (E) standard curves of $CD_{505\ nm}/CD_{650\ nm}$ responding to various concentrations of HClO; (F) T_1-weighted MRI images and (G) standard curves of T_1 value responding to various concentrations of HClO. (H) CD spectra and (I) statistic results of $CD_{505\ nm}/CD_{650\ nm}$ intensity ratio, (J) T_1-weighted MRI images, and (K) T_1 value of D-$Co(OH)_2$ NP responding to different excess interference and typical ROS *in vitro*. BSA: Bovine serum albumin; GSH: Glutathione; Glu: Glutamate; Gly: Glycine; SNOG: S-Nitrosylglutathione. Error bars are obtained from three parallel samples.

spectra exhibited approaching perfect mirror-symmetry for L-/D-$Co(OH)_2$ NPs, with two strong peaks at 340 mdeg (for L-$Co(OH)_2$ NPs) and 378 mdeg (for D-$Co(OH)_2$ NPs) at ~505 nm and 262 (for L-$Co(OH)_2$ NPs) and 265 (for D-$Co(OH)_2$ NPs) mdeg at 1100 nm (Figure 1C), while no CD signal was generated by achiral DL-aspartic acid coated $Co(OH)_2$ NPs (Figure S3A). The ultraviolet−visible absorption (UV−vis) spectra also showed a prominent peak around 505 nm and a weak peak at 1100 nm (Figures 1D and S3B). As shown in the *g*-factor (anisotropy factor, a dimensionless factor to assess the chiral optical activity intensity) spectra (Figure 1E), the maximum *g*-factor was 0.06 at around 1100 nm, thus suggesting that the $Co(OH)_2$ NPs had strong chiroptical activity. Furthermore, X-ray photoelectron spectra (XPS) were applied to evaluate the chemical composition of prepared chiral $Co(OH)_2$ NPs. By fitting the XPS spectrum (Figure 1F), we identified three strong binding energy peaks at 781.2 eV (Co^{2+} 2p 3/2), 796.4 eV (Co^{2+} 2p 1/2), and 802.2 eV (Co^{2+} 2p 1/2). The X-ray diffraction (XRD) results showed that the pattern was a hexagonal phase $Co(OH)_2$ (JCPDS No. 74-1057, Figure 1G). These results confirmed that chiral $Co(OH)_2$ NPs had been successfully synthesized via a gentle reaction method. Furthermore, the obtained chiral L-/D-$Co(OH)_2$ NPs exhibited broad optical absorption and strong CD signals in the visible and near-infrared regions. Therein, the origin of the chirality exhibited by L-/D-$Co(OH)_2$ NPs could be attributed to the widely accepted chirality transfer mechanism[41] in that the attached chiral ASP molecules were able to distort the crystal lattice in the vicinity of the surface of $Co(OH)_2$ NPs without the involvement of the central crystalline domains, thus inducing a strong chiroptical activity signal and showing that the racemic DL-aspartic acid was ineffective.

https://doi.org/10.1021/jacs.1c09986
J. Am. Chem. Soc. 2022, 144, 1580−1588

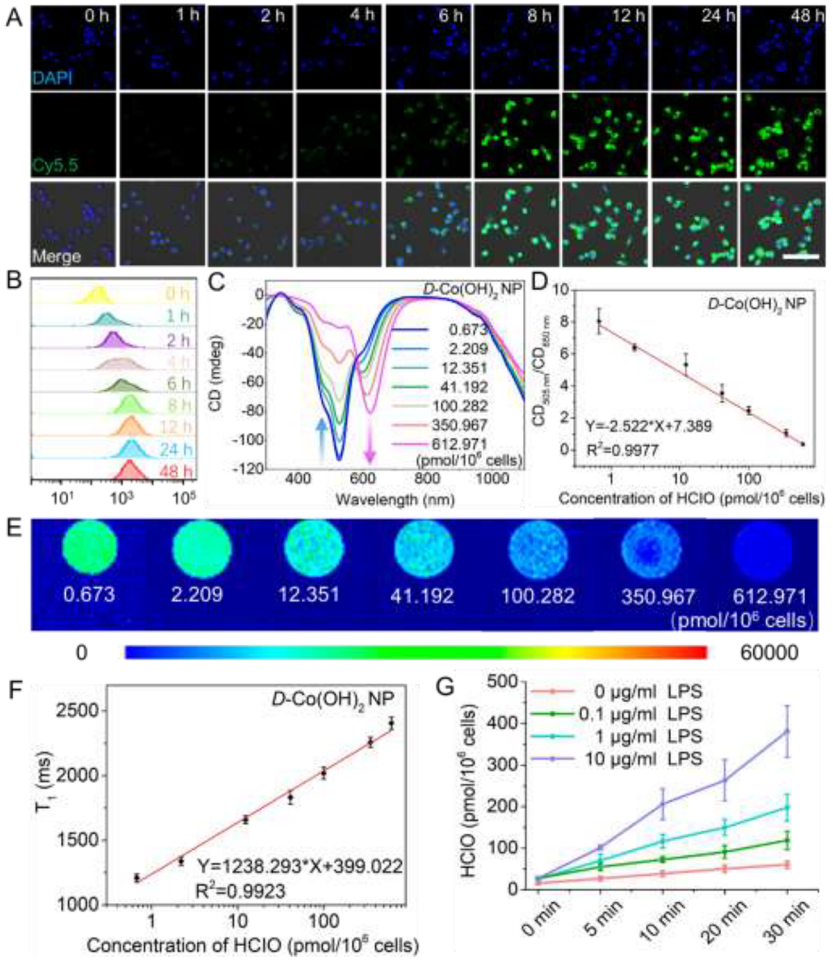

Figure 3. Dual-mode quantification and rapid monitoring HClO by CD and T_1-MRI signal of D-$Co(OH)_2$ NP in living cells. (A) Confocal images and (B) flow cytometry results of D-$Co(OH)_2$ NP modified with Cy5.5 as label for different incubation times with 4T1 cell lines. (C) CD spectra and (D) standard curves for $CD_{505\ nm}/CD_{650\ nm}$, (E) T_1-weighted MRI images, and (F) standard curves for T_1 value, of preincubated 4T1 cell lines with D-$Co(OH)_2$ NP and NAC further treated with different concentrations of HClO. (G) Quantification results of dynamic HClO level in 4T1 cell lines preincubated with D-$Co(OH)_2$ NP and NAC further treated with different concentrations of LPS to regulate the cellular oxidative stress level. Error bars are obtained from three parallel samples. Scale bar: 100 μm.

Reactions of Chiral $Co(OH)_2$ NPs to ROS. Due to the reduction of Co^{2+} and strong CD signals, chiral $Co(OH)_2$ NPs were initially expected to be oxidized reactively by high levels of oxidative ROS, thus enabling further quantification. To study this process, we selected HClO as a model for ROS in our following experiments. Unexpectedly, after the HClO addition, the CD peak of the chiral $Co(OH)_2$ NPs at approximately 505 nm evolved into a new weaker peak at 650 nm, with a corresponding change in CD values from 340 to 110 mdeg. Simultaneously, the CD peak at 1100 nm fell slightly from 260 to 180 mdeg (Figure 2A). Meanwhile, strong UV−vis absorption peak at 487 nm was also altered, and a broad absorption spectrum within the visible region was obtained (Figure S4A) as the maximum *g*-factor decreased from 0.06 to 0.05 (Figure S4B). These results indicated that the optical properties of the chiral $Co(OH)_2$ NPs changed significantly before and after the reaction with HClO. To identify the principle behind this process, the XPS spectrum of chiral $Co(OH)_2$ NPs was recorded after reacting with HClO. This allowed us to identify three binding energy peaks at 781.1 eV (Co^{3+} 2p 3/2), 781.5 eV (Co^{3+} 2p 3/2), and 805.2 eV (Co^{3+} 2p 1/2), thus exhibiting a higher molar ratio of Co^{3+} to Co^{2+} (Figure 2B). Furthermore, the Fourier-transform infrared (FTIR) spectra of chiral $Co(OH)_2$ NPs were compared before and after reacting with HClO (Figure S5). Three strong absorption peaks at 565, 690, and 1615 cm^{-1} were identified in the FTIR spectra after the chiral $Co(OH)_2$ NPs reacted with HClO. The former peak at 565 cm^{-1} could be assigned to Co^{3+}−O vibrations in the octahedrally coordinated metal ions. The band at 690 cm^{-1} was attributed to the stretching vibration mode of Co^{3+}−O in the tetrahedrally coordinated metal ions. The peak at 1615 cm^{-1} indicated the Co^{3+}−O double bond in the crystal structure of CoOOH. Thus, it could be verified by the XPS spectrum and FTIR spectra that Co^{2+} on the surface of the chiral $Co(OH)_2$ NPs was oxidized into Co^{3+} in the form of CoOOH by HClO, as follows:

$$Co(OH)_2 + HClO + e^- \rightarrow CoOOH + Cl^-$$

Meanwhile, the similar Raman bands in 1433 cm^{-1} representing the COO vibrational modes of the aspartic acid molecules, of D-$Co(OH)_2$ NP before and after reacting with HClO, was shown in Figure S6, suggesting that the chiral Asp molecules on the surface were not affected. Considering these data, we inferred that the mechanism underlying HClO-mediated CD spectra transformation, and the reduction in CD values, could be attributed to the partial oxidation of Co^{2+} into

https://doi.org/10.1021/jacs.1c09986
J. Am. Chem. Soc. 2022, 144, 1580−1588

Co^{3+} on the surface of the chiral $Co(OH)_2$ NPs, thus causing a variable coupling interaction between the chiral ligands and the inorganic core.[41]

Due to the innate magnetism of the cobalt atom[42−45] and the altered substance state in the above chemical reaction, we next performed MRI.[46] As shown in Figure 2C, the original red color of the T_1-weighted images of the chiral $Co(OH)_2$ NPs was weakened and became green in the presence of HClO. Furthermore, the T_1 value increased from 300 to 800 ms, thus representing a significant difference in relativity before and after the chiral $Co(OH)_2$ NPs reacted with HClO. Collectively, these results verified that an oxidation−reduction reaction occurred between the chiral $Co(OH)_2$ NPs and HClO, thus leading to changes in the chiroptical spectra and MRI signals generated by the chiral $Co(OH)_2$ NPs.

Selectivity and Sensitivity of Chiral $Co(OH)_2$ NPs for ROS. On the basis of the tunable CD and MRI signals that were associated with the oxidation reaction, we expected chiral $Co(OH)_2$ NPs to allow the effective quantification of ROS. Thus, the sensitivity and selectivity of chiral $Co(OH)_2$ NPs for ROS were examined based on the CD spectra and the T_1-MRI results. As shown in Figures 2D and S12, the CD signal intensity at ∼505 nm gradually declined from 340 mdeg (for L-$Co(OH)_2$ NPs) and 379 mdeg (for D-$Co(OH)_2$ NPs), and the peak at approximately 650 nm was simultaneously increased to 113 mdeg (for L-$Co(OH)_2$ NPs) and 114 mdeg (for D-$Co(OH)_2$ NPs) after reacting with increased concentrations of HClO. The reduced $CD_{505\ nm}/CD_{650\ nm}$ ratio of the chiral $Co(OH)_2$ NPs exhibited a perfect linear relationship with the HClO concentration ranging from 0.01 to 10 μM with an R^2 of 0.9928 and an LOD of 0.933 nM, thus suggesting an ultrasensitive response of the chiral $Co(OH)_2$ NPs to HClO (Figure 2E). With regards to MRI, we observed a color variation from red to green in the T_1-weighted images (Figure 2F), while the T_1 value increased linearly with the HClO concentration with an LOD of 1.367 nM (Figure 2G). Next, we evaluated the selectivity of chiral $Co(OH)_2$ NPs for ROS. In the presence of HClO and three other typical ROS, the CD intensity at 505 nm changed significantly with a corresponding reduction in the $CD_{505\ nm}/CD_{650\ nm}$ ratio. The T_1-weighted images exhibited a green color with an increasing T_1 value. No significant change was observed in terms of potential interfering components when compared with the blank group (Figure 2H−2K), thus confirming the well selectivity of the chiral $Co(OH)_2$ NPs to ROS. We ascribe this desirable selectivity to the oxidation-based mechanism of CD and MRI signal differences, in that reductants, nonoxidants, biomacromolecules, amino acids, typical reactive nitrogen species (RNS) and reactive sulfur species (RSS) in the system exert minimal interference upon the CD and MRI signal responses. Collectively, the chiral $Co(OH)_2$ NPs showed significant selectivity and sensitivity for the detection of ROS *in vitro*.

Dual-Mode Detection of ROS in Living Cells. Relying on the promising selectivity and sensitivity exhibited by CD and MRI mode, we anticipated that chiral $Co(OH)_2$ NPs would be able to quantify the levels of intracellular ROS. Before evaluating the performance of the chiral $Co(OH)_2$ NPs to detect ROS in living cells, we first tested the stability and cytotoxicity of chiral $Co(OH)_2$ NPs. There were no obvious differences in the CD spectra (Figure S7A), UV−vis absorption spectra (Figure S7B), or DLS results (Figure S8) after incubating the chiral $Co(OH)_2$ NPs for 48 h with cell medium, thus demonstrating good stability. Next, we tested cytotoxicity using the 4T1 cell line and observed good cell viability after incubating 100 μg/mL of chiral $Co(OH)_2$ NPs for 48 h, with results indicating that the D-$Co(OH)_2$ NPs showed a lower cell toxicity than L-$Co(OH)_2$ NPs (Figure S9). According to confocal results (Figures 3A and S10−S12) and flow cytometry results (Figures 3B and S13), 8 h was regarded as a balance time point during the cell uptake process of chiral $Co(OH)_2$ NPs. Therefore, we selected the 8 h time point for subsequent experiments and observed an astonishingly higher cell uptake efficiency for D-$Co(OH)_2$ NPs than for L-$Co(OH)_2$ NPs. On the basis of these results, we next used D-$Co(OH)_2$ NPs to detect intracellular levels of ROS.

Prior to detecting ROS in living cells, various concentrations of NaClO were added to increase intracellular HClO levels in the 4T1 cell line, a typical mouse breast cancer cell line with high expression levels of ROS. Cells were pretreated for 8 h with chiral $Co(OH)_2$ NPs and N-acetylcysteine (NAC) to eliminate intracellular ROS; and then, the intracellular levels of HClO were quantified with HClO assay kit. As the HClO levels increased, the CD spectra changed, as expected (Figures 3C and S14A), and a wide linear detection range (from 0.673 to 612.971 pmol/10^6 cells) was achieved in living cells, as based on the $CD_{505\ nm}/CD_{650\ nm}$ ratio (Figures 3D and S14B), with an LOD of 0.087 pmol/10^6 cells and 0.496 pmol/10^6 cells for D-$Co(OH)_2$ NPs and L-$Co(OH)_2$ NPs, respectively. For the MRI mode, we observed reduced intensity on T_1-weighted signal (Figures 3E and S14C) with the T_1 values showing a linear relationship with 0.179 pmol/10^6 cells and 0.633 pmol/10^6 cells LOD for D-$Co(OH)_2$ NPs and L-$Co(OH)_2$ NPs, respectively (Figures 3F and S14D). These results suggested that chiral $Co(OH)_2$ NPs exhibited a perfect tool for detecting ROS in living cells. Furthermore, an ∼5.7 times lower LOD was achieved in living cells, as shown by the CD signal of D-$Co(OH)_2$ NPs compared with L-$Co(OH)_2$ NPs. This could be attributed to a higher cellular accumulation of D-$Co(OH)_2$ NPs, thus representing a denser distribution than the L-$Co(OH)_2$ NPs in the intracellular microenvironment, thus creating a higher probability to react with randomly generated ROS and giving the D-$Co(OH)_2$ NPs a stronger capability to detect ROS at a lower concentration than L-$Co(OH)_2$ NPs.

On this basis, we considered whether D-$Co(OH)_2$ NPs could be used to monitor the variation in HClO levels due to its dynamic state in living cells. Thus, we carried out a series of experiments in the 4T1 cell line using D-$Co(OH)_2$ NPs (Figures 3G, S15, and S16). With an extended observation time, we observed increased HClO levels in 4T1 cell lines, as quantified by the D-$Co(OH)_2$ NPs. Following the stimulation of the 4T1 cell lines with increasing concentrations of lipopolysaccharide (LPS) to increase the level of oxidative stress,[47] we observed an upward trend for HClO, thus indicating that the D-$Co(OH)_2$ NPs could be used to track the *in situ* generation of HClO in living systems.

We also evaluated the versatility of D-$Co(OH)_2$ NPs in other cell lines. The HeLa cell line, macrophages cell (RAW 264.7) and primary uterine fibroblast (PCS-460-010) cell line, as typical human breast cancer cell line, inflammatory cell line, and normal cell line, respectively, were chosen to evaluate the detection performance of D-$Co(OH)_2$ NPs, along with 4T1 cell lines (Figure S17). For the HeLa cell lines, the intracellular ROS levels were calculated to be 172.53 ± 12.37 pmol/10^6 cells and 185.32 ± 22.15 pmol/10^6 cells from the CD mode and MRI mode, respectively. For the PCS-460−010 cell line, the CD and MRI detection results were 42.76 ± 4.14 pmol/

https://doi.org/10.1021/jacs.1c09986
J. Am. Chem. Soc. 2022, 144, 1580−1588

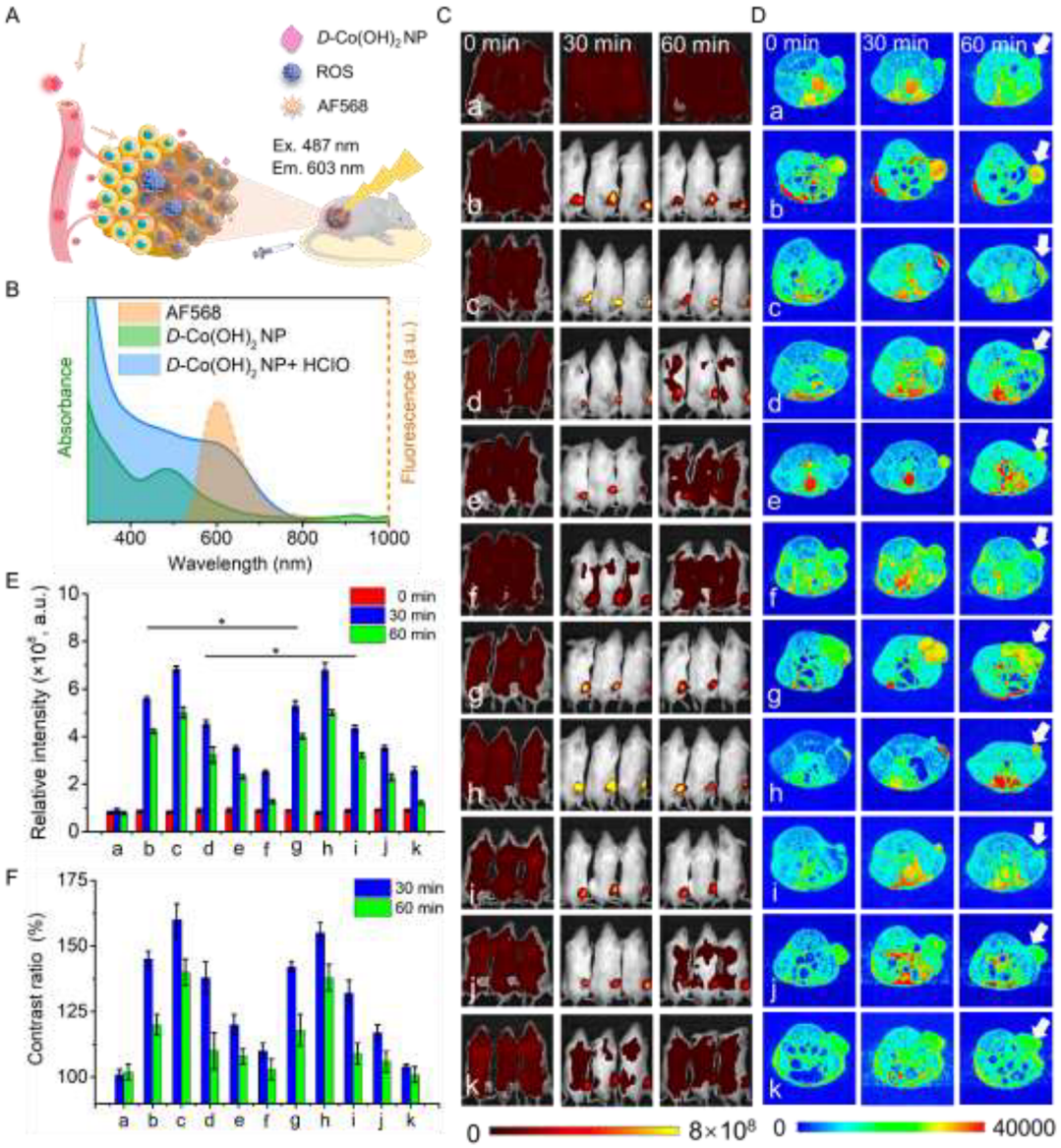

Figure 4. Application of chiral $Co(OH)_2$ NP *in vivo*. (A) Working process of ROS detection in tumor-bearing mice based on D-$Co(OH)_2$ NP. (B) UV−vis spectra for D-$Co(OH)_2$ NP before and after reacting with HClO, and fluorescence spectra of AF568 fluorescence molecules. (C) Fluorescence images and (D) MRI images for different treatment groups: (a) Saline, (b) D-$Co(OH)_2$ NP, (c) D-$Co(OH)_2$ NP + NAC, (d) D-$Co(OH)_2$ NP + LPS (10 mg/kg), (e) D-$Co(OH)_2$ NP + LPS (20 mg/kg), (f) D-$Co(OH)_2$ NP + LPS (40 mg/kg), (g) L-$Co(OH)_2$ NP, (h) L-$Co(OH)_2$ NP + NAC, (i) L-$Co(OH)_2$ NP + LPS (10 mg/kg), (j) L-$Co(OH)_2$ NP + LPS (20 mg/kg), (k) L-$Co(OH)_2$ NP + LPS (40 mg/kg), with different observation time, and corresponding statistic results of (E) relative fluorescence intensity and (F) contrast ratio for tumor site (white arrow) based on the ROI value in MRI images compared to a preinjection group, of 4T1 tumor-bearing mice for ROS detection by intravenously injecting chiral $Co(OH)_2$ NPs modified with AF568. Error bars are obtained from three parallel samples. *$P < 0.05$; one-way ANOVA, followed by Holm-Sidak post hoc test.

10^6 cells and 49.32 ± 5.33 pmol/10^6 cells, respectively. With regards to the 4T1 cell line, the CD and MRI detection results were 120.35 ± 6.86 pmol/10^6 cells and 129.32 ± 9.12 pmol/10^6 cells, respectively. We compared these results and found that they were consistent with those results using the commercial HClO kit, thus demonstrating that the D-$Co(OH)_2$ NPs exhibited satisfactory versatility in a range of cell lines.

Many probes have been developed to detect ROS;[48−50] however, these probes have not been able to accurately quantify intracellular ROS due to the complex cellular environment and the fragility of the probes. However, the fabricated D-$Co(OH)_2$ NPs described herein were shown to possess the ability to quantify intracellular levels of ROS with the lowest LOD of 0.087 pmol/10^6 cells (1.24 nM) when using CD signals (Table S1).

Chiral $Co(OH)_2$ NPs for Detecting ROS *in Vivo*. Although the detection of ROS in the living body remains a significant challenge, the well sensitivity and selectivity, low cytotoxicity, and high stability of our chiral $Co(OH)_2$ NP in living cells prompted us to investigate the *in vivo* performance of this novel nanoprobe. Hence, we tested the ability of the chiral D-/L-$Co(OH)_2$ NPs to detect ROS in tumor-bearing mice (Figure 4A). The imaging capability of the nanoprobe was a major factor to be considered in an *in vivo* sensor system. Thus, we first investigated fluorescence-based imaging *in vivo*.

https://doi.org/10.1021/jacs.1c09986
J. Am. Chem. Soc. 2022, 144, 1580−1588

The changes in the absorption peak for our chiral $Co(OH)_2$ NPs in the UV−vis spectrum before and after the reaction were used to regulate the fluorescence signal in a manner that was dependent on the spectrum overlap (Figure 4B). AF568 fluorescence molecules were employed to modify the NPs due to the fact that the maximum emission peak (603 nm) exhibited slightly overlap with the maximum UV−vis absorption peak of the original chiral $Co(OH)_2$ NPs (487 nm) to retain their fluorescence signals; however, after reacting $Co(OH)_2$ NPs with HClO, the overlap area between the emission spectra of AF568 fluorescence molecules and $Co(OH)_2$ NPs increased, resulting in fluorescence quenching by fluorescence resonance energy transfer, thus showing an "ON-OFF" fluorescence signal (Figure S18). Subsequently, we investigated the ROS quantification ability *in vivo* over a 60 min observation period using the chiral D-/L-$Co(OH)_2$ NPs modified with AF568. We used 4T1 tumor-bearing mice as a model in our experiments due to their high expression levels of ROS. We also used NAC as an antioxidant to downregulate ROS levels, and LPS as a pro-inflammatory cytokine inducer to gradually upregulate the ROS levels.[47] We also used saline injections in a control group to abolish signal interference in the living body caused by substances other than the chiral D-/L-$Co(OH)_2$ NPs. As shown in Figure 4C, the fluorescence signals from tumor-bearing mice treated with chiral $Co(OH)_2$ NPs were initially enhanced compared with the control group, but then diminished with time over the 60 min imaging period. In addition, an overall up-regulated fluorescence signal was detected in the group that was treated with NAC. In addition, a gradually quenched signal was detected at the tumor site in mice following treatment with increasing concentrations of LPS. Collectively, these results indicated that $Co(OH)_2$ NPs had the ability to detect ROS via a foreign fluorescence signal and showed a slightly higher relative fluorescence intensity in D-$Co(OH)_2$ NPs than in the L-$Co(OH)_2$ NPs. In addition, a similar signal change in MRI mode was also observed from the tumor site in MRI images and the region of interest (ROI) contrast ratio statistics results from tumor-bearing mice, thus indicating that natural MRI signals could be used to detect ROS (Figure 4D). And furthermore, D-$Co(OH)_2$ NPs showed a higher contrast ratio than L-$Co(OH)_2$ NPs due to the higher cellular uptake efficiency of D-$Co(OH)_2$ NPs (Figures S11). This may have caused the differences in fluorescence and MRI signals when compared with the L-$Co(OH)_2$ NPs, which was confirmed by analyzing the cobalt content at the tumor site and blood samples from tumor-bearing mice at different times (Figures 4E, 4F and S19). Accordingly, our chiral $Co(OH)_2$ NPs exhibited an effective ability to quantify ROS levels *in vivo* by both fluorescence and MRI signals.

We also tested the biosafety of chiral $Co(OH)_2$ NPs *in vivo*. We evaluated the acute toxicity of chiral $Co(OH)_2$ NPs over 72 h following intravenous injection. No significant differences were observed between the chiral $Co(OH)_2$ NPs group and the control group in terms of serum biochemistry tests (Figure S20). Furthermore, there were no obvious signs of inflammation or organ damage in the hematoxylin and eosin-stained images taken from the heart, liver, spleen, lung, and kidney (Figure S21), thus verifying the reliable biosafety of chiral $Co(OH)_2$ NPs. Collectively, these results demonstrated that chiral $Co(OH)_2$ NPs can be used as an operative and secure biosensor for the *in vivo* imaging and detection of ROS.

CONCLUSIONS

In summary, we fabricated a novel multimode chiral $Co(OH)_2$ NPs for ultrasensitive ROS profiling and monitoring in living cells and *in vivo*. Magneto-chiral $Co(OH)_2$ NPs can be synthesized gently and conveniently in aqueous solution, and possess strong optical activity and unique magnetic properties. Noticeably, magneto-chiral $Co(OH)_2$ NPs were demonstrated to exhibit reliable stability, high biocompatibility, and fine sensitivity and selectivity for ROS quantification based on an oxidation reaction in living cells and tumor-bearing mice. We also observed better detection performance for D-$Co(OH)_2$ NPs, due to the higher cellular accumulation compared to L-$Co(OH)_2$ NPs. In view of these advantages, magneto-chiral $Co(OH)_2$ NPs can be used for the real-time monitoring of ROS signaling events in biological systems as a high-performance tool in future research. The chirality-dependent detection performance of the developed $Co(OH)_2$ NPs can provide significant insight for designing the surface coating of probes using chiral molecules to further develop the bioapplication of these efficient probes.

ASSOCIATED CONTENT

Supporting Information

The Supporting Information is available free of charge at https://pubs.acs.org/doi/10.1021/jacs.1c09986.

Details on reagents, instruments, experimental sections including the synthesis procedures of chiral $Co(OH)_2$ nanoparticles, the cell viability test, the measurement methods of fluorescence and magnetic resonance imaging *in vitro* and *in vivo*, and the calculation method of limit of detection, as well as some additional supporting data (PDF)

AUTHOR INFORMATION

Corresponding Authors

Liguang Xu − *International Joint Research Laboratory for Biointerface and Biodetection, State Key Lab of Food Science and Technology, School of Food Science and Technology, Jiangnan University, Wuxi, Jiangsu 214122, P. R. China;* orcid.org/0000-0001-9453-7703; Email: xlg@jiangnan.edu.cn

Chuanlai Xu − *International Joint Research Laboratory for Biointerface and Biodetection, State Key Lab of Food Science and Technology, School of Food Science and Technology, Jiangnan University, Wuxi, Jiangsu 214122, P. R. China;* orcid.org/0000-0002-5639-7102; Email: xcl@jiangnan.edu.cn

Authors

Chen Li − *International Joint Research Laboratory for Biointerface and Biodetection, State Key Lab of Food Science and Technology, School of Food Science and Technology, Jiangnan University, Wuxi, Jiangsu 214122, P. R. China*

Si Li − *International Joint Research Center for Photo-responsive Molecules and Materials, School of Chemical and Material Engineering, Jiangnan University, Wuxi, Jiangsu 214122, P. R. China*

Jing Zhao − *Department of Radiology, Affiliated Hospital, Jiangnan University, Wuxi, Jiangsu 214122, P. R. China*

Maozhong Sun − *International Joint Research Laboratory for Biointerface and Biodetection, State Key Lab of Food Science*

and Technology, School of Food Science and Technology, Jiangnan University, Wuxi, Jiangsu 214122, P. R. China

Weiwei Wang − *International Joint Research Laboratory for Biointerface and Biodetection, State Key Lab of Food Science and Technology, School of Food Science and Technology, Jiangnan University, Wuxi, Jiangsu 214122, P. R. China*

Meiru Lu − *International Joint Research Laboratory for Biointerface and Biodetection, State Key Lab of Food Science and Technology, School of Food Science and Technology, Jiangnan University, Wuxi, Jiangsu 214122, P. R. China*

Aihua Qu − *International Joint Research Laboratory for Biointerface and Biodetection, State Key Lab of Food Science and Technology, School of Food Science and Technology, Jiangnan University, Wuxi, Jiangsu 214122, P. R. China*

Changlong Hao − *International Joint Research Laboratory for Biointerface and Biodetection, State Key Lab of Food Science and Technology, School of Food Science and Technology, Jiangnan University, Wuxi, Jiangsu 214122, P. R. China*

Chen Chen − *International Joint Research Laboratory for Biointerface and Biodetection, State Key Lab of Food Science and Technology, School of Food Science and Technology, Jiangnan University, Wuxi, Jiangsu 214122, P. R. China*

Hua Kuang − *International Joint Research Laboratory for Biointerface and Biodetection, State Key Lab of Food Science and Technology, School of Food Science and Technology, Jiangnan University, Wuxi, Jiangsu 214122, P. R. China;* orcid.org/0000-0002-2724-8722

Complete contact information is available at: https://pubs.acs.org/10.1021/jacs.1c09986

Author Contributions

[#]C.L., S.L., and J.Z. contributed equally to this paper.

Notes

The authors declare no competing financial interest.

■ ACKNOWLEDGMENTS

This work is financially supported by the National Natural Science Foundation of China (21977038, 51902136, 32071400) and Natural Science Foundation of Jiangsu Province (BK20180029).

■ REFERENCES

(1) Liu, Z.; Xiao, T. S. Partners with a Killer: Metabolic Signaling Promotes Inflammatory Cell Death. *Cell* **2021**, *184* (17), 4374−4376.

(2) Bazopoulou, D.; Knoefler, D.; Zheng, Y.; Ulrich, K.; Oleson, B. J.; Xie, L.; Kim, M.; Kaufmann, A.; Lee, Y. T.; Dou, Y.; Chen, Y.; Quan, S.; Jakob, U. Developmental ROS Individualizes Organismal Stress Resistance and Lifespan. *Nature* **2019**, *576* (7786), 301−305.

(3) Chen, X.; Wang, F.; Hyun, J. Y.; Wei, T.; Qiang, J.; Ren, X.; Shin, I.; Yoon, J. Recent Progress in the Development of Fluorescent, Luminescent and Colorimetric Probes for Detection of Reactive Oxygen and Nitrogen Species. *Chem. Soc. Rev.* **2016**, *45* (10), 2976−3016.

(4) Wang, X.; Zhong, X.; Bai, L.; Xu, J.; Gong, F.; Dong, Z.; Yang, Z.; Zeng, Z.; Liu, Z.; Cheng, L. Ultrafine Titanium Monoxide (TiO_{1+x}) Nanorods for Enhanced Sonodynamic Therapy. *J. Am. Chem. Soc.* **2020**, *142* (14), 6527−6537.

(5) Mao, D.; Hu, F.; Yi, Z.; Kenry, K.; Xu, S.; Yan, S.; Luo, Z.; Wu, W.; Wang, Z.; Kong, D.; Liu, X.; Liu, B. AIEgen-Coupled Upconversion Nanoparticles Eradicate Solid Tumors through Dual-Mode ROS Activation. *Sci. Adv.* **2020**, *6* (26), eabb271.

(6) Shao, Y.; Liu, B.; Di, Z.; Zhang, G.; Sun, L.; Li, L.; Yan, C. Engineering of Upconverted Metal−Organic Frameworks for Near-Infrared Light-Triggered Combinational Photodynamic/Chemo-/Immunotherapy against Hypoxic Tumors. *J. Am. Chem. Soc.* **2020**, *142* (8), 3939−3946.

(7) Tian, J.; Ding, L.; Xu, H. J.; Shen, Z.; Ju, H.; Jia, L.; Bao, L.; Yu, J. S. Cell-Specific and PH-Activatable Rubyrin-Loaded Nanoparticles for Highly Selective Near-Infrared Photodynamic Therapy against Cancer. *J. Am. Chem. Soc.* **2013**, *135* (50), 18850−18858.

(8) Yang, J.; Zhang, X.; Yuan, P.; Yang, J.; Xu, Y.; Grutzendler, J.; Shao, Y.; Moore, A.; Ran, C. Oxalate-Curcumin−Based Probe for Micro- and Macroimaging of Reactive Oxygen Species in Alzheimer's Disease. *Proc. Natl. Acad. Sci. U. S. A.* **2017**, *114* (47), 12384−12389.

(9) Hananya, N.; Green, O.; Blau, R.; Satchi-Fainaro, R.; Shabat, D. A Highly Efficient Chemiluminescence Probe for the Detection of Singlet Oxygen in Living Cells. *Angew. Chem., Int. Ed.* **2017**, *56* (39), 11793−11796.

(10) Zhao, J.; Gao, J.; Xue, W.; Di, Z.; Xing, H.; Lu, Y.; Li, L. Upconversion Luminescence-Activated DNA Nanodevice for ATP Sensing in Living Cells. *J. Am. Chem. Soc.* **2018**, *140* (2), 578−581.

(11) Wu, L.; Sedgwick, A. C.; Sun, X.; Bull, S. D.; He, X. P.; James, T. D. Reaction-Based Fluorescent Probes for the Detection and Imaging of Reactive Oxygen, Nitrogen, and Sulfur Species. *Acc. Chem. Res.* **2019**, *52* (9), 2582−2597.

(12) Tapeinos, C.; Pandit, A. Physical, Chemical, and Biological Structures Based on ROS-Sensitive Moieties that are able to Respond to Oxidative Microenvironments. *Adv. Mater.* **2016**, *28* (27), 5553−5585.

(13) Zhang, R.; Zhao, J.; Han, G.; Liu, Z.; Liu, C.; Zhang, C.; Liu, B.; Jiang, C.; Liu, R.; Zhao, T.; Han, M. Y.; Zhang, Z. Real-Time Discrimination and Versatile Profiling of Spontaneous Reactive Oxygen Species in Living Organisms with a Single Fluorescent Probe. *J. Am. Chem. Soc.* **2016**, *138* (11), 3769−3778.

(14) Chung, C. Y. S.; Timblin, G. A.; Saijo, K.; Chang, C. J. Versatile Histochemical Approach to Detection of Hydrogen Peroxide in Cells and Tissues Based on Puromycin Staining. *J. Am. Chem. Soc.* **2018**, *140* (19), 6109−6121.

(15) Wu, Z.; Liu, M.; Liu, Z.; Tian, Y. Real-Time Imaging and Simultaneous Quantification of Mitochondrial H_2O_2 and ATP in Neurons with a Single Two-Photon Fluorescence-Lifetime-Based Probe. *J. Am. Chem. Soc.* **2020**, *142* (16), 7532−7541.

(16) Li, Z.; Liang, T.; Lv, S.; Zhuang, Q.; Liu, Z. A Rationally Designed Upconversion Nanoprobe for in Vivo Detection of Hydroxyl Radical. *J. Am. Chem. Soc.* **2015**, *137* (34), 11179−11185.

(17) Liu, B.; Sun, Z.; Huang, P. J. J.; Liu, J. Hydrogen Peroxide Displacing DNA from Nanoceria: Mechanism and Detection of Glucose in Serum. *J. Am. Chem. Soc.* **2015**, *137* (3), 1290−1295.

(18) Zhang, P.; Wang, J.; Chen, H.; Zhao, L.; Chen, B.; Chu, C.; Liu, H.; Qin, Z.; Liu, J.; Tan, Y.; Chen, X.; Liu, G. Tumor Microenvironment-Responsive Ultrasmall Nanodrug Generators with Enhanced Tumor Delivery and Penetration. *J. Am. Chem. Soc.* **2018**, *140* (44), 14980−14989.

(19) Chen, T.; Hu, Y.; Cen, Y.; Chu, X.; Lu, Y. A Dual-Emission Fluorescent Nanocomplex of Gold-Cluster-Decorated Silica Particles for Live Cell Imaging of Highly Reactive Oxygen Species. *J. Am. Chem. Soc.* **2013**, *135* (31), 11595−11602.

(20) Kim, T. I.; Hwang, B.; Lee, B.; Bae, J.; Kim, Y. Selective Monitoring and Imaging of Eosinophil Peroxidase Activity with a J-Aggregating Probe. *J. Am. Chem. Soc.* **2018**, *140* (37), 11771−11776.

(21) Sedgwick, A. C.; Dou, W. T.; Jiao, J. B.; Wu, L.; Williams, G. T.; Jenkins, A. T. A.; Bull, S. D.; Sessler, J. L.; He, X. P.; James, T. D. An ESIPT Probe for the Ratiometric Imaging of Peroxynitrite Facilitated by Binding to Aβ-Aggregates. *J. Am. Chem. Soc.* **2018**, *140* (43), 14267−14271.

(22) Wang, X.; Sun, M.; Qu, A.; Wang, W.; Lu, M.; Guo, X.; Chen, C.; Hao, C.; Xu, L.; Xu, C.; Kuang, H. Improved Reactive Oxygen Species Generation by Chiral Co_3O_4 Supraparticles under Electromagnetic Fields. *Angew. Chem., Int. Ed.* **2021**, *60* (33), 18240−18246.

(23) Fan, J.; Kotov, N. A. Chiral Nanoceramics. *Adv. Mater.* **2020**, *32* (41), 1906738.

(24) Ma, W.; Xu, L.; De Moura, A. F.; Wu, X.; Kuang, H.; Xu, C.; Kotov, N. A. Chiral Inorganic Nanostructures. *Chem. Rev.* **2017**, *117* (12), 8041−8093.
(25) Gao, X.; Han, B.; Yang, X.; Tang, Z. Perspective of Chiral Colloidal Semiconductor Nanocrystals: Opportunity and Challenge. *J. Am. Chem. Soc.* **2019**, *141* (35), 13700−13707.
(26) Han, B.; Gao, X.; Lv, J.; Tang, Z. Magnetic Circular Dichroism in Nanomaterials: New Opportunity in Understanding and Modulation of Excitonic and Plasmonic Resonances. *Adv. Mater.* **2020**, *32* (41), 1801491.
(27) Lee, H.-E.; Ahn, H.-Y.; Mun, J.; Lee, Y. Y.; Kim, M.; Cho, N. H.; Chang, K.; Kim, W. S.; Rho, J.; Nam, K. T. Amino-Acid- and Peptide-Directed Synthesis of Chiral Plasmonic Gold Nanoparticles. *Nature* **2018**, *556* (7701), 360−365.
(28) Qu, A.; Sun, M.; Kim, J. Y.; Xu, L.; Hao, C.; Ma, W.; Wu, X.; Liu, X.; Kuang, H.; Kotov, N. A.; Xu, C. Stimulation of Neural Stem Cell Differentiation by Circularly Polarized Light Transduced by Chiral Nanoassemblies. *Nat. Biomed. Eng.* **2021**, *5* (1), 103−113.
(29) Kumar, J.; Eraña, H.; López-Martínez, E.; Claes, N.; Martín, V. F.; Solís, D. M.; Bals, S.; Cortajarena, A. L.; Castilla, J.; Liz-Marzán, L. M. Detection of Amyloid Fibrils in Parkinson's Disease Using Plasmonic Chirality. *Proc. Natl. Acad. Sci. U. S. A.* **2018**, *115* (13), 3225−3230.
(30) Jiang, W.; Qu, Z.; Kumar, P.; Vecchio, D.; Wang, Y.; Ma, Y.; Bahng, J. H.; Bernardino, K.; Gomes, W. R.; Colombari, F. M.; Lozada-Blanco, A.; Veksler, M.; Marino, E.; Simon, A.; Murray, C.; Muniz, S. R.; de Moura, A. F.; Kotov, N. A. Emergence of Complexity in Hierarchically Organized Chiral Particles. *Science* **2020**, *368* (6491), 642−648.
(31) Martens, K.; Binkowski, F.; Nguyen, L.; Hu, L.; Govorov, A. O.; Burger, S.; Liedl, T. Long- and Short-Ranged Chiral Interactions in DNA-Assembled Plasmonic Chains. *Nat. Commun.* **2021**, *12*, 2025.
(32) Lu, J.; Xue, Y.; Bernardino, K.; Zhang, N. N.; Gomes, W. R.; Ramesar, N. S.; Liu, S.; Hu, Z.; Sun, T.; de Moura, A. F.; Kotov, N. A.; Liu, K. Enhanced Optical Asymmetry in Supramolecular Chiroplasmonic Assemblies with Long-Range Order. *Science* **2021**, *371* (6536), 1368−1374.
(33) Hao, C.; Wu, X.; Sun, M.; Zhang, H.; Yuan, A.; Xu, L.; Xu, C.; Kuang, H. Chiral Core−Shell Upconversion Nanoparticle@MOF Nanoassemblies for Quantification and Bioimaging of Reactive Oxygen Species in Vivo. *J. Am. Chem. Soc.* **2019**, *141* (49), 19373−19378.
(34) Zhang, Q.; Hernandez, T.; Smith, K. W.; Hosseini Jebeli, S. A.; Dai, A. X.; Warning, L.; Baiyasi, R.; McCarthy, L. A.; Guo, H.; Chen, D.-H.; Dionne, J. A.; Landes, C. F.; Link, S. Unraveling the Origin of Chirality from Plasmonic Nanoparticle-Protein Complexes. *Science* **2019**, *365* (6460), 1475−1478.
(35) Wang, G.; Hao, C.; Ma, W.; Qu, A.; Chen, C.; Xu, J.; Xu, C.; Kuang, H.; Xu, L. Chiral Plasmonic Triangular Nanorings with SERS Activity for Ultrasensitive Detection of Amyloid Proteins in Alzheimer's Disease. *Adv. Mater.* **2021**, *33* (38), 2102337.
(36) Guo, X.; Sun, M.; Gao, R.; Qu, A.; Chen, C.; Xu, C.; Kuang, H.; Xu, L. Ultrasmall Copper (I) Sulfide Nanoparticles Prevent Hepatitis B Virus Infection. *Angew. Chem., Int. Ed.* **2021**, *60* (23), 13073−13080.
(37) Li, S.; Xu, L.; Ma, W.; Wu, X.; Sun, M.; Kuang, H.; Wang, L.; Kotov, N. A.; Xu, C. Dual-Mode Ultrasensitive Quantification of MicroRNA in Living Cells by Chiroplasmonic Nanopyramids Self-Assembled from Gold and Upconversion Nanoparticles. *J. Am. Chem. Soc.* **2016**, *138* (1), 306−312.
(38) Hou, K.; Zhao, J.; Wang, H.; Li, B.; Li, K.; Shi, X.; Wan, K.; Ai, J.; Lv, J.; Wang, D.; Huang, Q.; Wang, H.; Cao, Q.; Liu, S.; Tang, Z. Chiral Gold Nanoparticles Enantioselectively Rescue Memory Deficits in a Mouse Model of Alzheimer's Disease. *Nat. Commun.* **2020**, *11*, 4790.
(39) Sun, M.; Xu, L.; Qu, A.; Zhao, P.; Hao, T.; Ma, W.; Hao, C.; Wen, X.; Colombari, F. M.; de Moura, A. F.; Kotov, N. A.; Xu, C.; Kuang, H. Site-Selective Photoinduced Cleavage and Profiling of DNA by Chiral Semiconductor Nanoparticles. *Nat. Chem.* **2018**, *10* (8), 821−830.
(40) Yuan, A.; Hao, C.; Wu, X.; Sun, M.; Qu, A.; Xu, L.; Kuang, H.; Xu, C. Chiral Cu_xOS@ZIF-8 Nanostructures for Ultrasensitive Quantification of Hydrogen Sulfide In Vivo. *Adv. Mater.* **2020**, *32* (19), 1906580.
(41) Yeom, J.; Santos, U. S.; Chekini, M.; Cha, M.; De Moura, A. F.; Kotov, N. A. Chiromagnetic Nanoparticles and Gels. *Science* **2018**, *359* (6373), 309−314.
(42) Wang, J.; Jia, Y.; Wang, Q.; Liang, Z.; Han, G.; Wang, Z.; Lee, J.; Zhao, M.; Li, F.; Bai, R.; Ling, D. An Ultrahigh-Field-Tailored T_1−T_2 Dual-Mode MRI Contrast Agent for High-Performance Vascular Imaging. *Adv. Mater.* **2021**, *33* (2), 2004917.
(43) Wahsner, J.; Gale, E. M.; Rodríguez-Rodríguez, A.; Caravan, P. Chemistry of MRI Contrast Agents: Current Challenges and New Frontiers. *Chem. Rev.* **2019**, *119* (2), 957−1057.
(44) Ma, Y.; Yan, C.; Guo, Z.; Tan, G.; Niu, D.; Li, Y.; Zhu, W. H. Spatio-Temporally Reporting Dose-Dependent Chemotherapy via Uniting Dual-Modal MRI/NIR Imaging. *Angew. Chem., Int. Ed.* **2020**, *59* (47), 21143−21150.
(45) Zhao, Z.; Fan, H.; Zhou, G.; Bai, H.; Liang, H.; Wang, R.; Zhang, X.; Tan, W. Activatable Fluorescence/MRI Bimodal Platform for Tumor Cell Imaging via MnO_2 Nanosheet−Aptamer Nanoprobe. *J. Am. Chem. Soc.* **2014**, *136* (32), 11220−11223.
(46) Wu, L.; Wu, I. C.; Dufort, C. C.; Carlson, M. A.; Wu, X.; Chen, L.; Kuo, C. T.; Qin, Y.; Yu, J.; Hingorani, S. R.; Chiu, D. T. Photostable Ratiometric Pdot Probe for in Vitro and in Vivo Imaging of Hypochlorous Acid. *J. Am. Chem. Soc.* **2017**, *139* (20), 6911−6918.
(47) Zhu, H.; Fan, J.; Wang, J.; Mu, H.; Peng, X. An "Enhanced PET"-Based Fluorescent Probe with Ultrasensitivity for Imaging Basal and Elesclomol-Induced HClO in Cancer Cells. *J. Am. Chem. Soc.* **2014**, *136* (37), 12820−12823.
(48) Cheng, D.; Pan, Y.; Wang, L.; Zeng, Z.; Yuan, L.; Zhang, X.; Chang, Y.-T. Selective Visualization of the Endogenous Peroxynitrite in an Inflamed Mouse Model by a Mitochondria-Targetable Two-Photon Ratiometric Fluorescent Probe. *J. Am. Chem. Soc.* **2017**, *139* (1), 285−292.
(49) Zhang, X.-W.; Qiu, Q.-F.; Jiang, H.; Zhang, F.-L.; Liu, Y.-L.; Amatore, C.; Huang, W.-H. Real-Time Intracellular Measurements of ROS and RNS in Living Cells with Single Core-Shell Nanowire Electrodes. *Angew. Chem., Int. Ed.* **2017**, *56* (42), 12997−13000.
(50) Zhang, L.; Ma, C.; Sun, J.; Shao, B.; Portale, G.; Chen, D.; Liu, K.; Herrmann, A. Genetically Engineered Supercharged Polypeptide Fluids: Fast and Persistent Self-Ordering Induced by Touch. *Angew. Chem., Int. Ed.* **2018**, *57* (23), 6878−6882.

https://doi.org/10.1021/jacs.1c09986
J. Am. Chem. Soc. 2022, 144, 1580−1588